

Spin-polarized dynamic transport in tubular two-dimensional electron gases

E. A. Rothstein,^{1,*} B. Horovitz,¹ O. Entin-Wohlman,^{1,2} and A. Aharony^{1,2}

¹*Department of Physics, Ben Gurion University, Beer Sheva 84105, Israel*

²*Raymond and Beverly Sackler School of Physics and Astronomy, Tel Aviv University, Tel Aviv 69978, Israel*

(Dated: October 14, 2014)

The ac conductance of a finite tubular two-dimensional electron gas is studied in the presence of the Rashba spin-orbit interaction. When the tube is coupled to two reservoirs, that interaction splits the steps in the dc current, introducing energy ranges with spin-polarized currents. For this setup, we calculate the current-current correlations (the noise spectrum) and show that the existence of these dc spin-polarized currents can be deduced from the shot noise. We also find that the Wigner-Smith time delay is almost unaffected by the spin-orbit interaction. When the tube is coupled to a single reservoir, we calculate the quantum capacitance and the charge-relaxation resistance, and find that they exhibit singularities near the openings of new channels.

PACS numbers: 85.35.Kt, 72.10.-d, 72.70.+m, 42.50.Lc, 71.70.Ej

Keywords: quantum noise, core-shell nanowires, scattering mechanism, spin-orbit interaction

I. INTRODUCTION

Quite generally, the wavy nature of electrons together with the ensuing interference effects determine a large variety of quantum-coherence phenomena in quantum wires and dots. The electronic spin, being weakly coupled to other degrees of freedom in bulk materials, becomes an active player in these small systems.¹ This is due to the enhanced spin-orbit interaction induced by the Rashba effect,² that can be also modified experimentally.^{3,4} In multiply-connected mesoscopic systems, the effect of the spin-orbit interaction resembles that of an orbital magnetic field,⁵ paving the way to possible intriguing interference-induced outcomes.⁶ Indeed, there is an on-going vast experimental effort to study spin-orbit coupling effects in tubular systems, notably carbon nanotubes^{7,8} but also DNA and other long chiral molecules.⁹ However, the spin-orbit interaction in carbon nanotubes may not be predominantly of the Rashba type.¹⁰ It appears that core-shell semiconducting devices are more suitable to explore interference effects resulting from the Rashba spin-orbit coupling.

Core-shell nanowires comprise a thin layer (shell) surrounding a core in a tubular geometry.¹¹ While the charge carriers in these devices can be confined either to the core¹² or to the shell,¹³ it is clear that interference effects are more pronounced in the second case.¹⁴ Here we focus on this configuration, disregarding the core altogether. The electrical conductance of a finite-length tubular two-dimensional electron gas (2DEG) subject to the Rashba spin-orbit interaction has been analyzed exploiting scattering theory in the context of the Landauer formula.^{15,16} In this paper we study the frequency-dependent conductance of such a system, when it is connected to a tubular lead (or leads) where the electrons move ballistically. Measurements and calculations of the dynamic conductance supplement those of dc transport properties: while the latter yield the transmission of the mesoscopic system, the former contain in addition information related to the phases of the scattering matrix. The reason be-

ing that the ac quantities are given in terms of elements of the scattering matrix, and not only by their absolute values.

In the first part of the paper, Sec. II, we derive the dynamic conductance $\mathcal{G}(\omega)$ of a gated tubular 2DEG connected to a single electronic reservoir by a tubular lead (see Fig. 1) and study its low-frequency properties. This quantity, often referred to as admittance, is customarily presented in the form¹⁷

$$\mathcal{G}(\omega) \simeq -i\omega\mathcal{C} + \omega^2\mathcal{C}^2\mathcal{R}, \quad (1)$$

where ω is the frequency of the driving field. The expansion (1) introduces the “quantum capacitance” \mathcal{C} and the charge-relaxation resistance \mathcal{R} , both being topics of active research (see Sec. II). We present a detailed calculation of those for a tubular 2DEG, and in particular relate the capacitance to the Friedel phase and the charge accumulated in the tube. In the second part of the paper, Sec. III, the tubular 2DEG is connected to two reservoirs by two ballistic tubular leads, see Fig. 3. We calculate the various current-correlation functions, the shot noise and the Wigner-Smith time-delay matrix. In both Sec. II and Sec. III we first present the analytic expressions and then exemplify the results by several plots. The paper is supplemented by three appendices: the first details the derivation of the reflection matrix for the setup depicted in Fig. 1, the second discusses the limit where the scattering system is large enough for the frequency to exceed the level spacing, and the third gives the details of the calculation of the scattering matrix for the configuration shown in Fig. 3.

Our calculations are based on the scattering-matrix approach¹⁸ for noninteracting electrons. Electron-electron interactions are not taken into account; however, much of the physics in the Coulomb-blockade regime is believed to be captured by such models, with an effective Hartree-like energy¹⁹ (which can be incorporated into the our calculation quite easily). This simplification allows us to carry out the analysis analytically. Another major simplification stems from the geometry of the core-shell

systems: in a perfect tube, the linear Rashba spin-orbit interaction does not mix the transverse channels. For this reason, the effective magnetic field due to the spin-orbit coupling is in a sense analogous to that of an orbital magnetic field, similarly leading to interference phenomena.

Our research was motivated by the quest to detect hallmarks of the spin-orbit coupling in the ac properties of a mesoscopic conductor. The results in Sec. II show that the spin cannot be considered as another transport channel since the spin-orbit interaction mingles the two spin directions and causes a dependence of the quantization direction on the scattering energy. We also find there that the universal value of the charge-relaxation resistance predicted in Ref. 17 arises only when the transport occurs via the lowest-energy channel and is lost when higher-energy channels are included; this property, however, does not necessitate the spin-orbit coupling (though the latter does modify the results, see the discussion in Sec. II). In a way, the conclusions drawn in Sec. III are much more rewarding; in particular they indicate possibilities to induce and detect spin-polarized currents. The reason is related to the effect of the Rashba spin-orbit interaction on the transmission. As a function of the energy of the scattered electron, one of the spin channels may be blocked, and then the transmitted current is polarized.¹⁵ This is reflected in the dc conductance, and also in the shot noise (see Sec. III). We also find that this polarization can be manipulated by, e.g., a gate voltage. Thus, tubular core-shell systems appear to be interesting candidates for spintronic devices.

II. QUANTUM CAPACITANCE AND CHARGE-RELAXATION RESISTANCE

Ever since the experimental verification²⁰ of the prediction made in Ref. 17 (see also Refs. 21 and 22) concerning the universal value of the charge-relaxation resistance, there has been considerable interest in the low-frequency electrical properties of mesoscopic conductors. Here we examine those for a tubular mesoscopic conductor, in which spin-orbit interaction of the Rashba type is effective.

The system we study is depicted in Fig. 1: a mesoscopic cylinder, placed along the \hat{x} direction in the region $-d \leq x \leq 0$, is separated by a delta-function potential from the region $x \leq -d$ where the spin-orbit interaction vanishes and the electrons move ballistically. This potential is characterized by a single parameter ζ (measured in momentum units; units in which $\hbar = 1$ are used). When ζ is very large, the interface approaches the tunnel-junction limit. We assume that on the right (at $x \geq 0$) the cylinder is totally pinched off. Thus the system is described

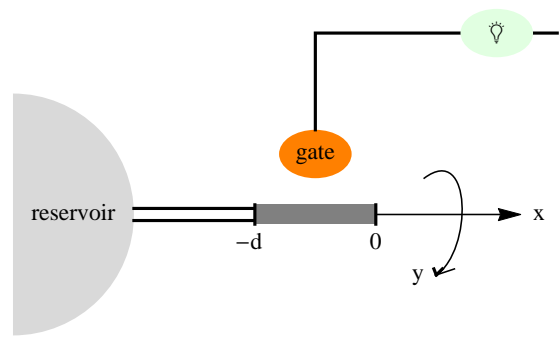


FIG. 1: (Color online) Tubular mesoscopic RC circuit. An ac source excites a periodic accumulation of charges on the gate, and the latter affects the charges on the mesoscopic cylinder (the dark region confined by the vertical thick lines) and thus creates an ac current flowing in the cylindrical lead (the light region of the tube) connecting the conductor to an electronic reservoir. A spin-orbit interaction of the Rashba type is operative in the mesoscopic cylinder, in the region $-d \leq x \leq 0$.

by the Hamiltonian

$$\mathcal{H} = \frac{1}{2m}(p_x^2 + p_y^2) + \frac{\zeta}{m}\delta(x+d) + \left(\Theta(-x)\Theta(x+d)\frac{\alpha}{2m}(p_y\sigma_x - p_x\sigma_y) + \text{Hc} \right), \quad (2)$$

where $\mathbf{p} = (p_x, p_y)$ is the two-dimensional momentum operator, α is the strength of the spin-orbit interaction (in momentum units) and $\sigma_{x,y}$ are the Pauli matrices. The coordinate system is specified in Fig. 1. Note that the hermitian conjugation in the last term of Eq. (2) yields a delta-function term, $-(\alpha/2m)\sigma_y\delta(x+d)$. This term is crucial for ensuring current continuity across the interface at $x = -d$.

The ac conductance of noninteracting electrons moving through a mesoscopic conductor can be presented in terms of the scattering matrix of the latter.^{17,22} For the setup displayed in Fig. 1, there is only a reflection matrix; its derivation is given in Appendix A. In this geometry, the wave vector along \hat{y} , denoted q , is fixed by the periodic boundary condition of this direction

$$q = \frac{2\pi n}{L}, \quad \text{with } n = 0, \pm 1, \pm 2, \dots, \quad (3)$$

where L is the circumference of the tube. The wave vector along the propagation direction \hat{x} is fixed by the energy E of the scattered electron. In the ballistic region it is

$$k = \sqrt{2mE - q^2}. \quad (4)$$

In the mesoscopic conductor where the spin-orbit interaction is effective it is expedient to measure the energy from $\alpha^2/(2m)$ (by adding this constant to the Hamiltonian of the scatterer). One finds that the longitudinal

wave vector takes two values,

$$k_{u,d} = \sqrt{(\sqrt{2mE} \pm \alpha)^2 - q^2} . \quad (5)$$

[The $+$ ($-$) sign belongs to k_u (k_d).] Note that while k_u is always real (since $q^2 \leq 2mE$), k_d may be purely imaginary and then one of the waves in the region $-d \leq x \leq 0$ is evanescent.^{15,23}

In our tubular geometry the transverse channels are not coupled, and the scattering matrix splits into blocks each describing the scattering matrix for a certain value of q , i.e., for a certain n . Due to the presence of the spin-orbit coupling spin is not conserved and therefore those blocks are 4×4 matrices. The reflection \mathbf{R} is hence a 2×2 matrix. We show in Appendix A that

$$\mathbf{R}(q) = [-1 + \mathbf{F}^{-1}(q)] , \quad (6)$$

where the matrix \mathbf{F} is too cumbersome to be reproduced here. It is shown in Appendix A that \mathbf{F} can be decomposed into

$$\mathbf{F}(q) = F_1(q) + \sigma_x F_x(q) + \sigma_z F_z(q) , \quad (7)$$

where the explicit expressions for the components are given in Eqs. (A9) and (A10). In particular, for $q = 0$ F_x and F_z vanish, and $\mathbf{R}_{q=0}$ is proportional to the unit matrix, i.e., the spin effects disappear. Indeed, when the energy of the scattered electron is too low to support a nonzero transverse mode, the motion becomes effectively one-dimensional and then the spin-orbit interaction can be eliminated by a gauge transformation,¹⁵ $\mathcal{U}\mathcal{H}\mathcal{U}^\dagger$, with $\mathcal{U} = \exp[-i\alpha\sigma_y x]$. This cancels the α -term in the Hamiltonian; the second boundary condition in Eqs. (A6) acquires then the term $\partial_x \mathcal{U}$ which cancels the $i\alpha\sigma_y$ term there.

The ac conductance in the linear-response regime, $\mathcal{G}(\omega)$, is given by

$$\mathcal{G}(\omega) = \frac{e^2}{2\pi} \int_{-\infty}^{\infty} dE \frac{f(E) - f(E + \omega)}{\omega} \times \sum_q \text{Tr}\{(1 - \mathbf{R}_q^\dagger(E)\mathbf{R}_q(E + \omega))\} , \quad (8)$$

where the trace is carried out in spin space. (It is written here in terms of the reflection alone; the more general form is given in Sec. III C.) The Fermi function, $f(E) = [\exp[(E - \mu)/(k_B T)] + 1]^{-1}$, describes the distribution of the electrons in the reservoir, with μ being the chemical potential there; below we confine our discussion to zero temperature and therefore μ is equal to the Fermi energy, $\mu = E_F$. The universal value of the charge-relaxation resistance discovered in Ref. 17 emerges upon comparing the low-frequency expansion of Eq. (8) [given in Eq. (1)] with the ac conductance,

$$\mathcal{G}_a(\omega) = -i\omega\mathcal{C} + \omega^2\mathcal{C}^2\mathcal{R} + \mathcal{O}(\omega^3) , \quad (9)$$

of a conventional capacitor whose capacitance is equal to \mathcal{C} and which is connected in series to a resistor whose

dc resistance is \mathcal{R} . For a single-channel scatterer, the reflection is just a phase factor, $\mathbf{R}(E) = \exp[i\phi(E)]$. One then finds for \mathcal{R} the value $\pi/(2e^2)$, half of the quantum unit of the resistance; it is independent of the scattering properties of the conductor. The capacitance, on the other hand, is given by $\mathcal{C} = (e^2/2\pi)\phi'(E_F)$, where ϕ' is the energy derivative of the reflection phase at the Fermi energy.

The case of the tubular conductor is different from the one treated in Ref. 17: first there are numerous transverse channels, and second there are the spin effects, rendering $\mathbf{R}(q)$ a unitary matrix (instead of being just a phase factor). Nonetheless, the capacitance can still be expressed in terms of phases. Indeed, the eigenvalues of $\mathbf{R}(q)$ are $\exp[i\phi_{1,2}]$ (for brevity we omit in some of the expressions the explicit dependence on q)

$$e^{i\phi_{1,2}} = -\left(1 - \frac{1}{\lambda_{1,2}}\right) , \quad (10)$$

where $\lambda_{1,2}$ are the eigenvalues of \mathbf{F} , Eq. (7),

$$\lambda_{1,2} = F_1 \pm \sqrt{F_1^2 - \det(\mathbf{F})} . \quad (11)$$

In particular we note that for the lowest transverse channel $q = 0$, the two eigenvalues are identical, $\phi_1(q = 0) = \phi_2(q = 0)$ (see the discussion in Appendix A). The quantum capacitance of the tubular 2DEG is given by

$$\mathcal{C} = \frac{e^2}{2\pi} \sum_q \left(\frac{\partial\phi_1(E, q)}{\partial E} + \frac{\partial\phi_2(E, q)}{\partial E} \right) \Big|_{E=E_F} . \quad (12)$$

On the other hand, the charge-relaxation resistance,

$$\mathcal{R} = \frac{e^2}{4\pi\mathcal{C}^2} \sum_q \text{Tr} \left(\frac{d\mathbf{R}^\dagger}{dE} \frac{d\mathbf{R}}{dE} \right) , \quad (13)$$

involves also the energy-derivatives of the quantization axis. This can be seen by presenting the reflection in the form

$$\mathbf{R} = e^{i\phi} e^{-i\theta\hat{\mathbf{n}}\cdot\boldsymbol{\sigma}} , \quad (14)$$

where $\boldsymbol{\sigma}$ is the vector of the Pauli matrices and the angles $\phi_{1,2}$, Eq. (10), are given by $\phi \pm \theta$. We show in Appendix A [see Eq. (A12)] that

$$\exp[i\phi] = \sqrt{\frac{\det(\mathbf{F}^*)}{\det(\mathbf{F})}} , \quad (15)$$

the unit vector $\hat{\mathbf{n}}$ (that depends on the energy), around which the spin rotates in spin space because of the spin-orbit coupling is the direction of the vector $(F_x, 0, F_z)$, and

$$\cos\theta = \frac{|F_1|^2 + F_x^2 + F_z^2}{\sqrt{(|F_1|^2 + F_x^2 + F_z^2)^2 - F_x^2 - F_z^2}} . \quad (16)$$

Exploiting the form Eq. (14) of the reflection matrix, one finds that

$$\text{Tr}\left(\frac{d\mathbf{R}^\dagger}{dE} \frac{d\mathbf{R}}{dE}\right) = \left(\frac{\partial\phi_1}{\partial E}\right)^2 + \left(\frac{\partial\phi_2}{\partial E}\right)^2 + 2\frac{\partial\hat{\mathbf{n}}}{\partial E} \cdot \frac{\partial\hat{\mathbf{n}}}{\partial E} \sin^2 \frac{\phi_1 - \phi_2}{2} \Big|_{E=E_F}. \quad (17)$$

The appearance of the last term in Eq. (17) is a direct result of the interference of the two spin directions. Obviously, the universal value of the charge-relaxation resistance that is independent of the details of the scatterer is obtained when the Fermi energy is so low that only the lowest transverse channel is excited. Then there remains only the $q = 0$ term in the sum, for which $\phi_1 = \phi_2$.

The capacitance \mathcal{C} may be related to the number, N_D , of displaced electrons around the scatterer (at energy E).¹⁷ According to the relation derived by Langer and Ambegaokar,²⁴ the Friedel sum-rule

$$N_D(E) = \frac{1}{2i\pi} \text{Tr} \ln[\mathbf{R}(E)], \quad (18)$$

gives N_D in terms of the *full* reflection (see also Ref. 25). By exploiting the identity $\ln \det(\mathbf{M}) = \text{Tr} \ln \mathbf{M}$ where \mathbf{M} is an arbitrary matrix, we find

$$\begin{aligned} N_D(E) &= \frac{1}{2i\pi} \ln \prod_q e^{i[\phi_1(E,q) + \phi_2(E,q)]} \\ &= \frac{1}{2\pi} \sum_q [\phi_1(E,q) + \phi_2(E,q)]. \end{aligned} \quad (19)$$

Comparing Eq. (19) with Eq. (12) shows that

$$\mathcal{C} = e^2 \frac{dN_D}{dE}, \quad (20)$$

in agreement with Ref. 17 (see the discussion at the end of Appendix A). However, $N_D(E)$, as well as its energy derivative, are meaningful only when the scattering phases are measured outside the system, typically asymptotically,^{24,25} whereas we measure our phases relative to $x=-d$; this definition may cause the capacitance to attain negative values (see Appendix A).

The quantum capacitance and the charge-relaxation resistance are plotted in Figs. 2 as a function of the Fermi energy. The striking aspect of these figures are the sharp extrema in both the quantum capacitance and the charge-relaxation resistance, albeit the rather low barrier between the scatterer and the lead ($\zeta=0.6$ in the figure). The ones in the capacitance (see the upper panel in Fig. 2) correspond to the standing waves in the tube (when detached). An intriguing point is the negativity of \mathcal{C} near the second step for $\alpha = 0.2$ (in units of L^{-1}). The appearance of negative values depends on the choice of parameters and also on the point along the $\hat{\mathbf{x}}$ -axis relative to which the phase is measured. The latter feature implies that some charge has been displaced to the range $x < -d$. Also note that the vanishing of \mathcal{C} leads to formally a diverging \mathcal{R} , yet the measurable quantity [as well

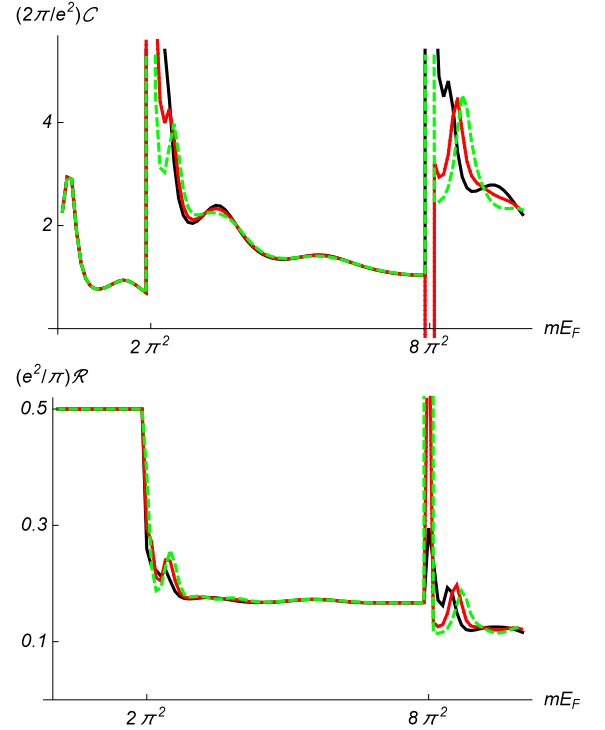


FIG. 2: (Color online) Upper panel: the quantum capacitance, Eq. (12); lower panel: the charge-relaxation resistance, Eq. (13), as a function of the Fermi energy (normalized by m , in units of L^{-2}) and $\zeta = 0.6$ (in units of L^{-1}). The solid (black) curve is for $\alpha = 0.1$, the smaller-dashed (red) one is for $\alpha = 0.2$, and the large-dashed (green) curve is for $\alpha = 0.3$ (in units of L^{-1}). In all our figures $d = L$.

as the expansion parameter in Eq. (1)] is $\mathcal{C}^2\mathcal{R}$, which is finite when $\mathcal{C} = 0$. The charge-relaxation resistance itself is a useful object when it is quantized (below the first step) or nearly quantized (not too close to other steps).

The resistance for $n = 0$ (i.e., for $q = 0$) is constant, reflecting the universal value of the charge-relaxation resistance discussed above. For finite values of q [i.e., $n \neq 0$, Eq. (3)] the “base line” of the charge-relaxation resistance is approximately at $\mathcal{R} = \pi/[2(2n+1)e^2]$, as if comprising $2n+1$ resistors in parallel, of magnitude $\pi/(2e^2)$ each, in agreement with Büttiker *et al.*²¹ (recall the degeneracy of q). The spin-orbit coupling removes the degeneracy of the longitudinal wave function, and causes (when strong enough, see the large-dashed curve in Fig. 2) the splitting of the second peak of \mathcal{R} .

We note in passing that the measured capacitance is different from \mathcal{C} as defined in Eq. (12).^{17,26} There the capacitance is deduced from the current response dI at the lead (at $-\infty$) to the voltage dV relative to the potential on the probed region dU , i.e. $dI = \mathcal{G}(\omega)(dV - dU) = -i\omega\mathcal{C}(dV - dU) + \mathcal{O}(\omega^2)$. On the other hand, the measured capacitance \mathcal{C}_m is defined by $dI = -i\omega\mathcal{C}_m(dV - dV')$ where dV' is the potential change on a gate near the probed region. The potential change dV' generates locally a change in the charge

such that $dI = -i\omega\mathcal{C}_e(dU - dV')$ where \mathcal{C}_e is known as the geometric capacitance. Eliminating dU one finds that $1/C_m = 1/C_e + 1/C$.^{17,26}

The low-frequency expansion leading to Eq. (12) for the capacitance and Eq. (13) for the charge-relaxation resistance has to be handled cautiously when the scattering tube is long enough for the frequency to exceed the level spacing, $md^2 \gg \omega^{-1}$. The reason is that then the reflection matrix elements [as a function of E , $E + \omega$, see Eq. (8)] are wildly oscillating. We examine this case in Appendix B (ignoring the spin-orbit interaction for simplicity); in particular we show that the charge-relaxation resistance of the lowest transverse mode is $2\pi/(2e^2)$, in agreement with Refs. 27.

III. THE NOISE SPECTRUM

A. General expressions

Here we study the current-correlation functions, i.e., the noise spectrum of a tubular 2DEG subject to the Rashba interaction, see Fig. 3. The tube is placed along the $\hat{\mathbf{x}}$ -direction and we include in the analysis the orbital effect of a magnetic field along $\hat{\mathbf{x}}$, which might add versatility to the device. The magnetic field is specified by a flux Φ penetrating the cylinder. The Rashba-affected tubular 2DEG, confined to the region $|x| \leq d$, is separated from the cylindrical leads by two tunnel junctions characterized by ζ_L and ζ_R for the left and the right barrier, respectively (in units of momentum). These leads are coupled each to an electronic reservoir, where the electronic distribution is

$$f_\gamma(E) = [e^{\beta(E-\mu_\gamma)} + 1]^{-1}, \quad \gamma = L \text{ or } R, \quad (21)$$

with μ_γ being the chemical potential in reservoir γ . We assume that the reservoirs are not spin polarized, and therefore the Fermi functions do not depend on the spin index.

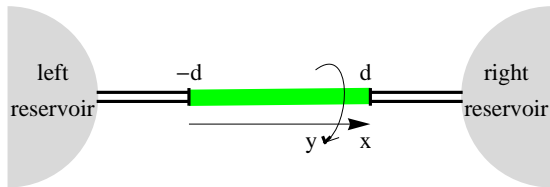


FIG. 3: (Color online) A tubular mesoscopic conductor [the dark (green) part of the cylinder] is connected to two reservoirs via leads (the light parts of the tube) where the electrons move ballistically. The region where spin-orbit interaction is active ($|x| < d$) is separated from the leads by two potential barriers (thick vertical lines). A magnetic field along $\hat{\mathbf{x}}$ adds to the versatility of the device.

The Hamiltonian describing this setup is

$$\mathcal{H} = \frac{1}{2m}(p_x^2 + p_y^2) + \frac{\zeta_L}{m}\delta(x+d) + \frac{\zeta_R}{m}\delta(x-d) + \frac{\alpha}{2m}\left(\Theta(d-|x|)(p_y\sigma_x - p_x\sigma_y) + \text{Hc}\right). \quad (22)$$

Once again we measure the energy E in the region $|x| \leq d$ with respect to $\alpha^2/(2m)$ [see comment after Eq. (4)]. The presence of a magnetic field along $\hat{\mathbf{x}}$ modifies the y component of the momentum, $p_y \rightarrow p_y - A_y$, where $A_y = e\Phi/(cL)$ is the vector potential in units of inverse length. As a result, the wave vector q along $\hat{\mathbf{y}}$ given in Eq. (3) is modified as well, $q \rightarrow q - \varphi$, where $\varphi \equiv A_y$. Below, we keep the notation q for the transversal momentum, bearing in mind the shift caused by the magnetic flux. The current-current correlations (i.e., the noise spectrum) are expressed in terms of the scattering matrix of the scatterer, i.e., the $|x| \leq d$ region.¹⁸ This matrix, pertaining to the Hamiltonian (22), is derived in Appendix C.

Within the scattering formalism, the time-dependent operator of the current leaving lead χ , $\hat{I}_\chi(t)$ is¹⁸ ($\chi = L$ or R)

$$\hat{I}_\chi(t) = \frac{e}{2\pi} \sum_{\tilde{\sigma}} \int_{-\infty}^{\infty} dE \int_{-\infty}^{\infty} dE' e^{i(E-E')t} \times \sum_{\gamma, \gamma'} \sum_{\sigma, \sigma'} \sum_q [A_{\gamma\sigma; \gamma'\sigma'}(\chi\tilde{\sigma}, E, E') \hat{a}_{\gamma, \sigma}^\dagger(E) \hat{a}_{\gamma', \sigma'}(E')] . \quad (23)$$

The summation over the spin index $\tilde{\sigma}$ indicates that Eq. (23) pertains to the total electric current (as opposed to the spin-resolved one¹⁵). The indices γ, σ (γ', σ') and the argument E (E') specify a scattering state of energy E (E') excited by an electron of spin polarization σ (σ') incoming from lead γ (γ') with $\gamma, \gamma' = L$ or R .¹⁵ The fermionic operators $\hat{a}_{\gamma, \sigma}^\dagger(E)$ and $\hat{a}_{\gamma, \sigma}(E)$ create and annihilate an electron in the corresponding scattering state. These operators are normalized such that

$$\langle \hat{a}_{\gamma\sigma}^\dagger(E) \hat{a}_{\gamma'\sigma'}(E') \rangle = \delta_{\gamma\gamma'} \delta_{\sigma\sigma'} \delta(E-E') f_\gamma(E) . \quad (24)$$

The matrix \mathbf{A} is given in terms of the scattering matrix, \mathcal{S} .¹⁸ In the tubular geometry considered here the transverse modes are not coupled, and therefore the scattering matrix splits into blocks of 4×4 matrices for each value of the transverse momentum q [see Eq. (C6)]; we omit the argument q from \mathbf{A} for brevity]. For each value of q the elements of the (4×4) matrix \mathbf{A} are given by

$$A_{\gamma\sigma; \gamma'\sigma'}(\chi\tilde{\sigma}, E, E') = \delta_{\gamma\gamma'} \delta_{\sigma\sigma'} \delta_{\chi\gamma} \delta_{\tilde{\sigma}\sigma} - \mathcal{S}_{\chi\tilde{\sigma}; \gamma\sigma}^*(E) \mathcal{S}_{\chi\tilde{\sigma}; \gamma'\sigma'}(E') , \quad (25)$$

where \mathcal{S} is derived in Appendix C [see in particular Eq. (C6)].

The dc current through the scatterer is readily obtained by averaging Eq. (23) using Eq. (24). This leads to the celebrated Landauer formula²⁸ for the net current

in terms of the transmission

$$I \equiv \langle \hat{I}_L \rangle = -\langle \hat{I}_R \rangle \\ = \frac{e}{2\pi} \int_{-\infty}^{\infty} dE [f_L(E) - f_R(E)] \mathcal{T}(E), \quad (26)$$

where the transmission \mathcal{T} is

$$\mathcal{T}(E) = \sum_q \mathcal{T}_q(E) = \sum_q \text{Tr}[\mathbf{T}_{LR,q}^\dagger(E) \mathbf{T}_{LR,q}(E)]. \quad (27)$$

Here the trace is carried out in spin space; the (2×2) matrix \mathbf{T}_{LR} (as well as the other matrices comprising the q -dependent scattering matrix) is given in Eqs. (C7).

As usual, we present the current correlations in the frequency domain, by defining²⁸

$$\mathcal{K}_{\chi\chi'}(\omega) = \int_{-\infty}^{\infty} dt e^{i\omega t} \langle \delta \hat{I}_\chi(t) \delta \hat{I}_{\chi'}(0) \rangle, \quad (28)$$

with $\delta \hat{I}_\chi(t) = \hat{I}_\chi(t) - \langle \hat{I}_\chi \rangle$.

Upon exploiting the relations (23) and (24) we find¹⁸

$$\mathcal{K}_{\chi\chi'}(\omega) = \frac{e^2}{2\pi} \int_{-\infty}^{\infty} dE \sum_{\gamma\gamma'} f_\gamma(E) [1 - f_{\gamma'}(E + \omega)] \sum_q \sum_{\sigma\sigma'\tilde{\sigma}} A_{\gamma\sigma;\gamma'\sigma'}(\chi\tilde{\sigma}, E, E + \omega) A_{\gamma'\sigma';\gamma\sigma}(\chi'\tilde{\sigma}, E + \omega, E). \quad (29)$$

Inspecting Eq. (29), one can distinguish between two types of correlations, the auto-correlations, for which $\chi = \chi'$, and the cross correlations, where $\chi \neq \chi'$. For instance, when the setup is not biased, i.e., $\mu_L = \mu_R$, the auto-correlation spectrum is given by

$$\mathcal{K}_{RR}(\omega) = \frac{e^2}{2\pi} \int_{-\infty}^{\infty} dE f(E) [1 - f(E + \omega)] \sum_q \text{Tr}[2 - \mathbf{R}_{RR}^\dagger(E) \mathbf{R}_{RR}(E + \omega) - \mathbf{R}_{RR}^\dagger(E + \omega) \mathbf{R}_{RR}(E)], \quad (30)$$

where the trace is carried out in spin space, and the (2×2) matrix \mathbf{R} is given in Eqs. (C7). Likewise, the cross-correlation function for $\mu_L = \mu_R$ is

$$\mathcal{K}_{LR}(\omega) = \frac{e^2}{2\pi} \int_{-\infty}^{\infty} dE f(E) [1 - f(E + \omega)] \sum_q \text{Tr}[\mathbf{T}_{LR}^\dagger(E) \mathbf{T}_{LR}(E + \omega) + \mathbf{T}_{LR}^\dagger(E + \omega) \mathbf{T}_{LR}(E)]. \quad (31)$$

When the junction is symmetric, i.e., the two tunnel junctions on both its sides are of identical strength $\zeta_L = \zeta_R$ then $\mathcal{K}_{LL}(\omega) = \mathcal{K}_{RR}(\omega)$ and $\mathcal{K}_{LR}(\omega) = \mathcal{K}_{RL}(\omega)$. Otherwise, the expressions for \mathcal{K}_{LL} and \mathcal{K}_{RL} are obtained from Eqs. (30) and (31) upon interchanging L with R .

The correlations of the physical quantities are combinations of the auto- and cross- correlations. For instance, since the operator of the net current through the scatterer, \hat{I} , reads

$$\hat{I}(t) = [\hat{I}_L(t) - \hat{I}_R(t)]/2, \quad (32)$$

it is evident from Eq. (29) that the correlation of the net current is given by $[\mathcal{K}_{LL} + \mathcal{K}_{RR} - \mathcal{K}_{LR} - \mathcal{K}_{RL}]/4$. Likewise, the charge correlation is²⁹ $[\mathcal{K}_{LL} + \mathcal{K}_{RR} + \mathcal{K}_{LR} + \mathcal{K}_{RL}]/4$. In particular, in the zero-frequency limit the net-current correlation is the shot noise, which is given by [see Eq. (29)]

$$\mathcal{K}_s = \frac{e^2}{2\pi} \int_{-\infty}^{\infty} dE \sum_{\gamma=L,R} \left(f_\gamma(E) [1 - f_\gamma(E)] \text{Tr}\{\mathcal{T}(E)^2\} + f_\gamma(E) [1 - f_{\bar{\gamma}}(E)] \text{Tr}\{\mathcal{T}(E) [1 - \mathcal{T}(E)]\} \right), \quad (33)$$

where $\bar{\gamma}$ is the lead opposite to the γ lead. This result extends the celebrated expression first derived in Ref. 30 to include the effects of spin-orbit interaction.

B. Results

In the absence of the spin-orbit interaction, the magnetic field, and the potential barriers at $x = \pm d$ (see Fig. 3), the transmission (27) of the tubular 2DEG exhibits the well-known phenomenon of perfect conductance quantization, whose hallmark is the staircase structure of the conductance (or the transmission) as a func-

tion of the Fermi energy (i.e., the gate voltage). Indeed, in this quintessential configuration the transmission amplitude matrices \mathbf{T}_{LR} and \mathbf{T}_{RL} [see Eqs. (C7)] are both given by a unit matrix times $\exp[2id\sqrt{2mE - q^2}]$, opening a new transverse channel whenever E is large enough for an additional q to yield a real k [see Eq. (4)]. Note though, that as opposed to a flat two-dimensional wire, here the quantization steps appear for $n = 2, 6, 10$, etc.¹⁵

[see Eq. (3)] reflecting the helical degeneracy of the q values for the cylinder. Since the conductor is perfectly transmitting, the shot noise Eq. (33) vanishes; the auto- and cross- correlations do not. For instance, at zero temperature and for an un-biased system, $\mu_L = \mu_R = E_F$, Eqs. (30) and (31) yield

$$\begin{aligned} \frac{\pi}{2e^2} \mathcal{K}_{RR}(\omega) &= \omega, \quad \text{per channel}, \\ \frac{\pi}{2e^2} \mathcal{K}_{LR}(\omega) &= \int_{E_F - \omega}^{E_F} dE \sum_q \\ &\times \cos[2d(\sqrt{2mE - q^2} - \sqrt{2m(E + \omega) - q^2})]. \end{aligned} \quad (34)$$

The fact that the current correlations do not vanish for an un-biased conductor at zero temperature reflects the relation between the noise spectrum and the absorption/emission capacity of the scattering system.^{31,32} These results are exemplified in Fig. 4 by the solid (blue) curves.

The spin-orbit interaction lifts partially the helical degeneracy. As mentioned, one of the longitudinal wave vectors, k_d , can become imaginary. This happens when $2mE < (q + \alpha)^2$; in that case the corresponding wave is evanescent and does not contribute to the transmission [recall that energy is measured from $\alpha^2/(2m)$]. As a result, the conductance steps are split¹⁵ (save the first one, which, as explained above, is insensitive to the spin-orbit interaction). Moreover, since the transmission is not perfect anymore, the shot noise (as a function of the bias) is finite. As can be seen in the mid panel of Fig. 4, the shot noise begins at small bias voltages V with a nearly horizontal slope, corresponding to a fully-transmitting channel. It then develops a steeper slope, reflecting the partially-transmitting channel (*cf.* the top panel). The fact that each stair (save the very first one) is split into two means that in the low-energy part of the stair only one of the spinors is propagating (the other belongs to the evanescent wave); in other words, the electric current is spin polarized.¹⁵

The effect of the spin-orbit coupling on the shot noise is better appreciated from Fig. 5, where it is plotted (as a function of the bias voltage) for various values of the coupling strength α (in units of inverse length). Grossly speaking, the staircase structure is gradually lost as the spin-orbit coupling increases. Perhaps the main feature of the shot noise brought about by the spin-orbit interaction is the division between regions in which it is roughly horizontal and where it is approximately linearly increasing. The first pertains to the case in which both spinors are transmitted, while the second describes the situation where one of the spinors is blocked. In this way, the shot noise may serve as an indicator for a spin-polarized current.

It is also of interest to explore the effect of a gate voltage applied uniformly on the scatterer. To this end we add to the Hamiltonian (22) the term $U\Theta(d - |x|)$. The gate potential U which acts as a potential well/wall modifies the width of the conductance stairs. As men-

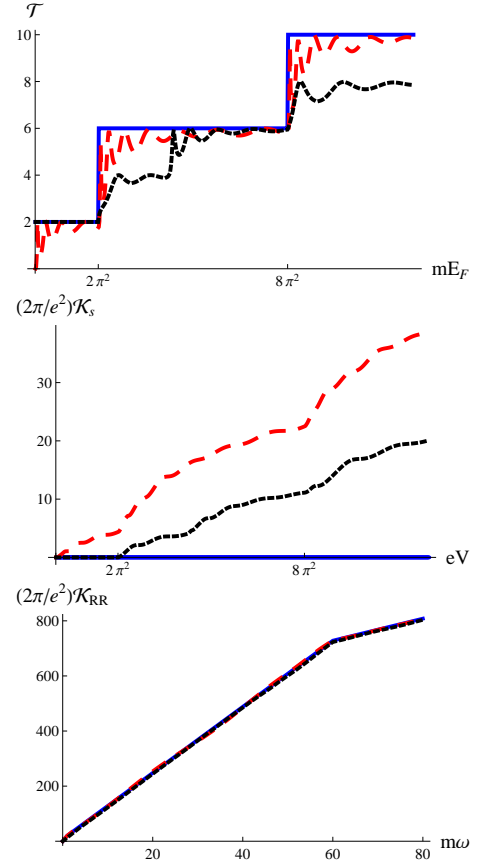


FIG. 4: (Color online) Top: the transmission as a function of the Fermi energy; mid panel: the shot noise Eq. (33) as a function of the bias voltage $eV = \mu_L - \mu_R$; bottom: the auto-correlation Eq. (30) as a function of the external frequency (both the energy and the frequency are normalized by the mass m and are measured in units of L^{-2}). The thin solid (blue) line in the top panel corresponds to the perfect conductor, in the absence of the spin-orbit coupling, the dotted (black) curve is for the case $\alpha = 0.9\pi$ and no potential barriers at the two ends, $\zeta_L = \zeta_R = 0$, and the dashed (red) curve is for $\zeta_L = \zeta_R = 1.2$, in units of L^{-1} . In the bottom panel $E_F = 80$ in units of mL^{-2} ; the solid (blue) and the dotted (black) curves there overlap.

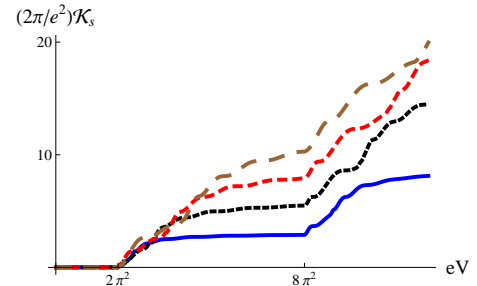


FIG. 5: (Color online) The shot noise as a function of bias voltage, for a completely open cylinder, $\zeta_L = \zeta_R = 0$. The solid (blue) curve is for $\alpha = 0.2\pi$, the dotted (black) one is for 0.4π , the small-dashed (red) line is for 0.6π , and the large-dashed (brown) line is for 0.8π ; all in units of L^{-1} .

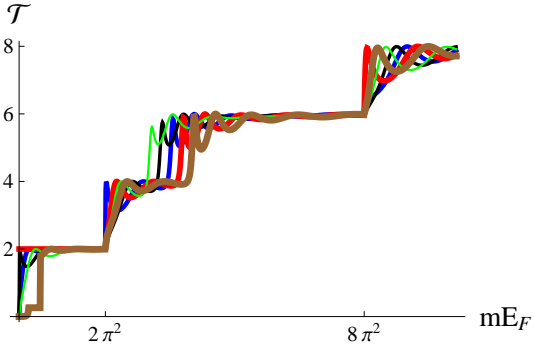


FIG. 6: (Color online) The transmission as a function of the Fermi energy. The various curves are for different values of the gate voltage U (see text). In increasing order of the thickness, the thinnest (blue) curve is for $U = 0$, then, $mU = -(0.7\pi)^2/2$ (black), $mU = (0.7\pi)^2/2$ (red), $mU = -(0.7\pi)^2$ (green), and the thickest $mU = (0.7\pi)^2$ (brown), in units of L^{-2} . Here $\alpha = 0.7\pi$, and $\zeta_L = \zeta_R = 0$.

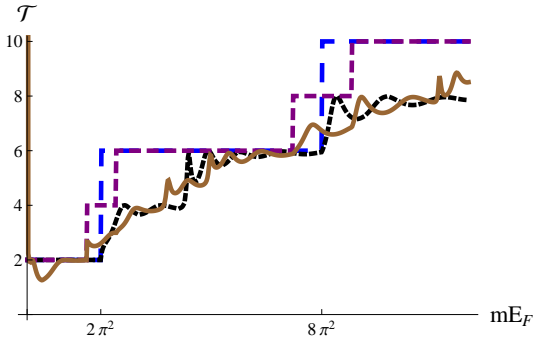


FIG. 7: (Color online) The transmission as a function of the Fermi energy. The largest-dashed and the dotted curves (blue and black) are the same as in Fig. 4, and are reproduced here as a reference. The solid and small-dashed lines (brown and purple) exhibit the effect of a magnetic flux (we use $\varphi = 0.2\pi$). The staircase one (purple) is for $\alpha = 0$, the wavy one (brown) is for $\alpha = 0.9\pi$ in units of L^{-1} .

tioned above, the spin-orbit interaction splits each conductance/transmission stair into two; the width (in energy) of the split step is $q^2 - 2\alpha|q| \leq 2m(E_F - U) \leq q^2 + 2\alpha|q|$, for $2mU \geq 2\alpha|q|$. This behavior is depicted in Fig. 6. The width may then be controlled by the gate voltage; in view of the comments above (in conjunction with Fig. 4) we conclude that by varying the gate voltage one may manipulate the spin polarization of the electric current.

Another tool to lift the helical degeneracy is to apply a magnetic flux along the tube axis. In the absence of the flux, the scattering states for n and for $-n$ are degenerate [n is the quantum number of the transverse modes, see Eq. (3)]. The magnetic flux removes this degeneracy, as illustrated in Fig. 7, turning the 4-fold degeneracy into a two-fold one. The reason being the modification of the transverse wave vector q by the relative flux φ , $q \rightarrow q - \varphi$, as discussed after Eq. (22). Thus for ex-

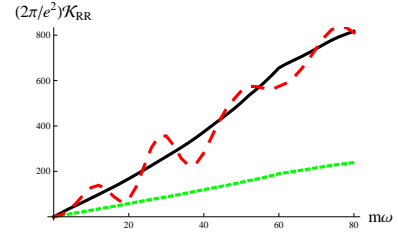


FIG. 8: (Color online) The auto-correlation noise, $\mathcal{K}_{RR}(\omega)$, as a function of frequency (normalized by the mass m and measured in units of L^{-2}), for $\alpha = 3.1\pi$ (in units of L^{-1}). The solid (black) reference curve corresponds to $\zeta_L = \zeta_R = 0$, the dotted (green) line is for $\zeta_L = 1.2$ and $\zeta_R = 19.2$, while the dashed (red) line is for $\zeta_L = 19.2$ and $\zeta_R = 1.2$, all in units of L^{-1} .

ample, the threshold for the opening of a new step in the transmission is $2mE_F > \min(q - \varphi)^2$, where “min” stands for the minimal value of $(q - \varphi)^2$ for all q -values. Under the action of both a magnetic field and the spin-orbit coupling, the entire 4-fold degeneracy is removed, as shown by the thick, very wavy (brown) curve in Fig. 7. It follows that manipulating the gate voltage and the magnetic field in a Rashba scatterer enables a good control on both the helicity and the spin degrees of freedom of the transmitted electrons.

We now turn to discuss the current-correlation functions [see e.g., Eqs. (30) and (31)]. These are known to be rather sensitive to asymmetries of the setup, in our case to a possible difference between ζ_L and ζ_R .^{29,33} Figure 8 displays the auto-correlation \mathcal{K}_{RR} , in the absence of the spin-orbit coupling and a bias voltage. There is a distinct disparity between \mathcal{K}_{RR} pertaining to the case where the left tunnel junction is almost pinched off (the wavy line) and when it is almost open (the lower thick line; the thin line is for $\zeta_L = \zeta_R = 0$, and serves as a reference) where the noise is considerably lower. The auto-correlation decreases as ζ_R increases, and vanishes when this tunnel junction is pinched off.

C. The Wigner-Smith time-delay matrix

We conclude this section with a discussion of the Wigner-Smith time-delay matrix of our core-shell structure. Smith³⁴ introduced the time-delay hermitian matrix

$$\tau_{\gamma\gamma'}(E_F) = \sum_q \text{Tr} \left(\frac{1}{2\pi i} \mathbf{S}_{\gamma\gamma'}^\dagger(E) \frac{d\mathbf{S}_{\gamma\gamma'}(E)}{dE} \right) \Big|_{E_F}, \quad (35)$$

whose diagonal matrix elements measure the average lifetime of a scattering event (the collision lifetime in the terminology of Ref. 34). Here $\gamma, \gamma' = L, R$, and \mathbf{S} is the scattering matrix pertaining to a certain value of q (see Appendix C). Explicitly, $\tau_{\gamma\gamma'}(E_F)$ is the time delay experienced by an electron at the Fermi energy incident from the γ lead into the γ' one (including in our case all

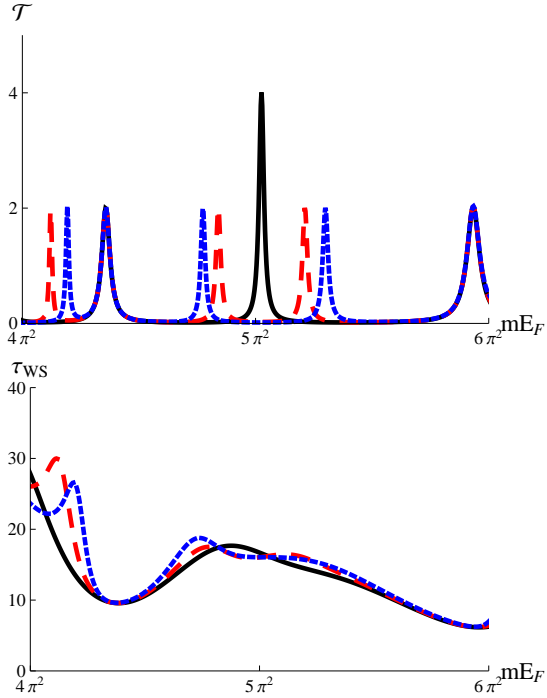


FIG. 9: (Color online) The upper panel displays the transmission as a function of the Fermi energy (in units of L^{-2}) and the lower panel shows the Wigner-Smith time (in units of \hbar), again as a function of the Fermi energy. Here $d = 1$ (in units of L), $\phi = 0$, and $\zeta = 30$ (in units of L^{-1}). The solid (black) curve is for $\alpha = 0$, the dotted one (blue) one is for $\alpha = 0.2\pi$, and the dashed line (red) curve is for $\alpha = 0.1\pi$.

transverse channels and the spin polarizations) because of the scatterer. This quantity is intimately related to the quantum capacitance studied in the previous section, and is also related to the thermopower the scatterer is capable of producing.³⁵ Indeed, by expanding the dynamic conductance¹⁷ $\mathcal{G}_{\gamma\gamma'}(\omega)$

$$\mathcal{G}_{\gamma\gamma'}(\omega) = \frac{e^2}{2\pi} \int \frac{dE}{\omega} [f(E) - f(E + \omega)] \times \sum_q \text{Tr}[\delta_{\gamma\gamma'} - \mathbf{S}_{\gamma\gamma'}^\dagger(E) \mathbf{S}_{\gamma\gamma'}(E + \omega)], \quad (36)$$

to first order in the external frequency ω , one finds that at zero temperature

$$\mathcal{G}_{\gamma\gamma'}(\omega) \simeq \mathcal{G}_{\gamma\gamma'}(0) - ie^2 \omega \tau_{\gamma\gamma'}. \quad (37)$$

For $\gamma \neq \gamma'$, e.g., $\gamma = L$ and $\gamma' = R$, the first term on the right-hand side of Eq. (37) is the transmission given in Eq. (27) times the quantum unit of the conductance $[e^2/(2\pi)]$ for a single spin, with $\hbar = 1$, i.e., the Landauer conductance. The simple separation of the ac conductance into real and imaginary parts which appears in Eq. (37) led to the identification of the quality factor of the mesoscopic conductor as roughly the absolute value of the ratio $\text{Im}\mathcal{G}/\text{Re}\mathcal{G}$.³⁶ (Reference 36 replaces the denominator by the number of channels up to the Fermi energy. This replacement is apparently valid when the transmission is close to resonance.) The quality factor measures the capability of a circuit to store energy; its enhanced value in carbon nanotubes is a subject of current interest.³⁷ Our analysis below is carried out for an “average delay time”, τ_{WS} , defined by

$$\tau_{WS} = \frac{2\pi}{\mathcal{T}} \sum_{\gamma, \gamma'} \tau_{\gamma\gamma'}. \quad (38)$$

Note that τ_{WS} is measured in units of \hbar .

As explained by Smith,³⁴ close to resonance the delay time is related to the (inverse of the) resonance width. In fact, when the scattering matrix can be described by a simple Breit-Wigner resonance of width Γ , τ_{WS} as defined in Eq. (38) equals Γ^{-1} . In an attempt to investigate this feature in a core-shell system, we confine ourselves in this subsection to high tunnel barriers such that the transmission consists of narrow peaks. (For simplicity a symmetric setup where $\zeta_L = \zeta_R \equiv \zeta$ is considered.) Figures 9 and 10 display (in the upper panels) the transmission as a function of the Fermi energy around one of the (relatively) sharp peaks (the higher is ζ , the sharper are the transmission peaks), and in the lower panels the corresponding Wigner-Smith time, Eq. (38). As can be expected, the average delay time does vary with the Fermi energy, though the transmission is close to resonance. An example is shown in Fig. 9. The full (black) curves in the two panels there are the transmission and τ_{WS} in the absence of the spin-orbit coupling. It is rather straightforward to find that for $\alpha = 0$

$$\mathcal{T} = \sum_q \left(1 + 4 \frac{\zeta^2}{k^2} [k \cos(2kd) + \zeta \sin(2kd)]^2 \right)^{-1}, \quad (39)$$

where q and k are given by Eqs. (3) and (4), respectively, and

$$\tau_{WS} = \frac{1}{\mathcal{T}} \sum_q \frac{8d}{v(E_F)} \frac{1 + \frac{\zeta}{k^2 d} + \frac{2\zeta^2}{k^2} + \frac{2\zeta^2}{k^4 d} \sin(2kd) [\zeta \sin(2kd) + k \cos(2kd)]}{1 + 4 \frac{\zeta^2}{k^2} [k \cos(2kd) + \zeta \sin(2kd)]^2}, \quad (40)$$

where $v(E_F) \equiv k/m$ is the velocity of the electron at

the Fermi energy. For instance, when $\zeta = 0$ Eq. (40)

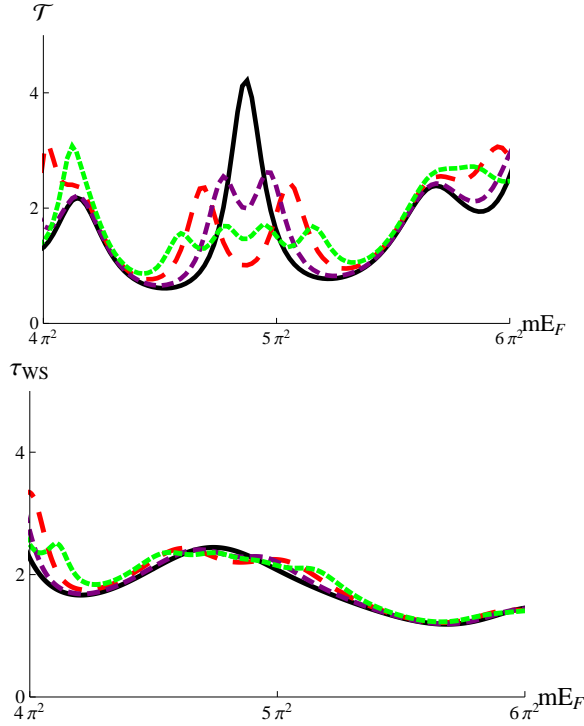


FIG. 10: (Color online) The upper panel is the transmission and the lower panel is τ_{WS} , both as a function of the Fermi energy. Here $d = 1$ (in units of L) and $\zeta = 9.7$ (in units of L^{-1}). The solid (black) curve is for $\alpha = \phi = 0$, the small-dashed (purple) curve is for $\alpha = 0.1\pi$ and $\phi = 0$, the large-dashed curve (red) is for $\alpha = 0$ and $\phi = 0.05\pi$, and the dotted (green) one is for $\alpha = 0.1\pi$ and $\phi = 0.05\pi$.

gives for τ_{WS} the value $4 \times 2d/v(E_F)$, which is the time required for an electron to traverse ballistically a tube of length $2d$, times the spin and helical degeneracies.

Figure 9 displays the Wigner-Smith time for a rather sharp transmission peak. The curves are for different values of the spin-orbit coupling; it is seen that while this coupling has a substantial effect on the transmission by removing the spin degeneracy (splitting the peak into two), it hardly changes τ_{WS} . The same feature can be observed in Fig. 10; there we have added the effect of the magnetic flux, which lifts the helical degeneracy. Nonetheless, the Wigner-Smith time is almost unchanged. Comparing the two figures, 9 and 10, it is observed that (not surprisingly) τ_{WS} increases significantly as the transmission peak becomes narrower.

IV. CONCLUSIONS

We have investigated several frequency-dependent properties of a tubular two-dimensional electron gas, subject to the Rashba spin-orbit interaction. In this quintessential geometry the spin-orbit coupling does not mix the transverse channels, and therefore the effect of the interaction can be related to interference.

We have found that when the tubular two-dimensional electron gas is coupled to a single reservoir the quantum capacitance \mathcal{C} and the charge-relaxation resistance \mathcal{R} are sensitive probes of the charging state of the scatterer. In particular peaks in \mathcal{C} correspond to resonance states (standing waves of the isolated segment) while peaks in \mathcal{R} correspond to minima of \mathcal{C} [as expected from Eqs. (12) and (13)] in between the peaks of \mathcal{C} or at zeroes of \mathcal{C} (see Figs. 2); an exception is the $q = 0$ case where \mathcal{R} attains the universal value $\pi/(2e^2)$.

For the tubular system with two reservoirs we find that the interference related to the spin-orbit coupling is in particular manifested in the upper panel of Fig. 10, where we see the similar manner by which both an orbital magnetic field (directed along the axis of the tube) and the spin-orbit coupling (that can also be assigned an effective magnetic field; the interference effect of the spin-orbit interaction is mainly due to the effective field associated with the transverse direction, i.e., along the \hat{x} -direction) affect the transmission. The other remarkable effect of the spin-orbit coupling is its capability to block one of the propagating spinors in each transverse channel.^{15,23} In the case of the transmission, this is translated into splitting of the stairs (as a function of the Fermi energy, and for not too strong α). In the case of the shot noise, this blocking modifies the shot noise as a function of the bias voltage. Since when one of the propagating spinors is blocked the current is spin-polarized, measurements of the conductance and the shot noise can indicate the range of Fermi energies where this polarization takes place.

Acknowledgments

This work was supported by the Israeli Science Foundation (ISF), by the Infrastructure program of Israeli Ministry of Science and Technology under the contract 3-11173, and the US-Israel Binational Science Foundation (BSF).

Appendix A: The reflection matrix (Fig. 1)

The scattering matrix for the geometry of Fig. 1 is reduced to a reflection matrix; for instance, in the absence of the spin-orbit interaction and the delta-function potential at the interface $x = -d$ it is proportional to the unit matrix (suitably choosing the origin). In order to derive it, we write for the wave function the Ansatz

$$\varphi_b(x, y) = \sum_q e^{iqy} (e^{ikx} |c_{in}\rangle + e^{-ikx} |c_{out}\rangle), \quad (A1)$$

in the ballistic region $x \leq -d$, and

$$\varphi_t(x, y) = \sum_q e^{iqy} (\mathbf{v}_u e^{ik_u x \sigma_z} |c_u\rangle + \mathbf{v}_d e^{ik_d x \sigma_z} |c_d\rangle), \quad (A2)$$

in the mesoscopic conductor, in the region $-d \leq x \leq 0$. Here σ_z is the third Pauli matrix. Equation (A2) is valid for positive values of q , Eq. (3); a similar calculation holds for the negative values. The matrices \mathbf{v}_u and \mathbf{v}_d are

$$\mathbf{v}_u = \begin{bmatrix} v_u & -v_u^{-1} \\ -v_u^{-1} & v_u \end{bmatrix}, \quad \mathbf{v}_d = \begin{bmatrix} v_d & v_d^{-1} \\ v_d^{-1} & v_d \end{bmatrix}, \quad (\text{A3})$$

with

$$v_{u,d} = \left(\frac{q + ik_{u,d}}{q - ik_{u,d}} \right)^{\frac{1}{4}}. \quad (\text{A4})$$

The various coefficients in Eqs. (A1) and (A2) are obtained by imposing boundary conditions. Explicitly

$$\mathbf{v}_u |c_u\rangle + \mathbf{v}_d |c_d\rangle = 0, \quad (\text{A5})$$

to ensure the vanishing of φ_t at $x = 0$, and

$$\begin{aligned} \varphi_b(-d, y) &= \varphi_t(-d, y), \\ \left(\frac{\partial \varphi_b(x, y)}{\partial x} - \frac{\partial \varphi_t(x, y)}{\partial x} \right) \Big|_{x=-d} &= 2\zeta \varphi_b(-d, y) + i\alpha \sigma_y \varphi_b(-d, y), \end{aligned} \quad (\text{A6})$$

for continuity at $x = -d$. Using Eqs. (A5) and (A6) to eliminate the vectors $|c_{u,d}\rangle$ results in the relation

$$e^{-ikd} |c_{in}\rangle = \mathbf{F}(e^{-ikd} |c_{in}\rangle + e^{ikd} |c_{out}\rangle), \quad (\text{A7})$$

$$\mathbf{F} = F_1 + \sigma_x F_x + \sigma_z F_z, \quad (\text{A8})$$

with

$$\begin{aligned} F_1 &= \frac{1}{2} + \frac{i\zeta}{k} + \frac{i}{\Omega} \left(k_d \cos(dk_d) \sin(dk_u) [2\alpha\sqrt{2mE} + 4mE] + k_u \sin(dk_d) \cos(dk_u) [4mE - 2\alpha\sqrt{2mE}] \right), \\ F_x &= \frac{2iq\sqrt{2mE}}{\Omega} \left(k_d \cos(dk_d) \sin(dk_u) - k_u \sin(dk_d) \cos(dk_u) \right), \\ F_z &= \frac{iq}{\Omega} \left(2[k^2 + \alpha^2] \sin(dk_d) \sin(dk_u) + 2k_d k_u [\cos(dk_d) \cos(dk_u) - 1] \right). \end{aligned} \quad (\text{A9})$$

Here we have defined

$$\Omega = 4k \left([2mE + q^2 - \alpha^2] \sin(dk_u) \sin(dk_d) + k_d k_u [1 - \cos(dk_d) \cos(dk_u)] \right). \quad (\text{A10})$$

Finally we note that in the first transverse channel, i.e., for $q = 0$, F_x and F_z vanish, while

$$F_1 = \frac{1}{2} + \frac{i\zeta}{k} + \frac{i(k_u + k_d) \cot[\frac{1}{2}(k_u + k_d)d]}{4k}. \quad (\text{A11})$$

Note that in order to obtain Eq. (6) from Eq. (A7) we have shifted the origin by $-d$, i.e., $\exp[ikd]|c_{out}\rangle \rightarrow |c_{out}\rangle$ and $\exp[-ikd]|c_{in}\rangle \rightarrow |c_{in}\rangle$.

As mentioned in the text, k_d can be either real or imaginary. However, in both cases F_x and F_z are purely imaginary, and $F_1 + F_1^* = 1$. These properties ensure that the reflection matrix $\mathbf{R}(q)$ [see Eq. (6)] is unitary. [The condition $\mathbf{F} + \mathbf{F}^\dagger = 1$ (for each value of q) is dictated by the optical theorem.] A straightforward algebra gives that for each value of q the reflection matrix is given by

$$\begin{aligned} \mathbf{R} &= \sqrt{\frac{[F_1^*]^2 - F_x^2 - F_z^2}{F_1^2 - F_x^2 - F_z^2}} \\ &\times \frac{|F_1|^2 + F_x^2 + F_z^2 - \boldsymbol{\sigma} \cdot (F_x, 0, F_z)}{\sqrt{(|F_1|^2 + F_x^2 + F_z^2)^2 - F_x^2 - F_z^2}}, \end{aligned} \quad (\text{A12})$$

which leads to the form (14) used in Sec. II.

We have chosen \mathbf{R} to define the reflection at $x = -d$. This choice, which is not so benign, reflects our expectation that the displacement of the electrons [see Eq. (18)] is confined to the range $-d < x < 0$ so that the quantum capacitance, Eq. (20), will be positive. We have seen, however, that very close to the singular steps this may not be the case. Negative capacitance has been given various interpretations³⁸, while here it reflects the spatial range of charge response. Ideally one could measure the whole wire and then the capacitance would be always positive and Eq. (20) would become exact.

We end this appendix by listing the explicit analytical expressions for the scattering phases for the case where the spin-orbit coupling vanishes. Then the eigenvalues of the matrix \mathbf{F} , Eq. (11), and the corresponding phases Eq. (10), are

$$\lambda_1 = \lambda_2 = \frac{1}{2} + i\frac{\zeta}{k} + \frac{i}{2} \cot k, \quad (\text{A13})$$

and

$$e^{i\phi_1} = e^{i\phi_2} = e^{2ikd} \frac{\zeta(1 - e^{-2idk}) + ik}{\zeta(1 - e^{2idk}) - ik}, \quad (\text{A14})$$

with

$$\begin{aligned} \frac{\partial \phi_1}{\partial E} &= \frac{m}{k} \left(2d \right. \\ &\quad \left. + \frac{-4\zeta \sin(kd)[(2d\zeta - 1) \sin(kd) + 2kd \cos(kd)]}{4\zeta^2 \sin(2kd) + 2\zeta k \sin(2kd) + k^2} \right). \end{aligned} \quad (\text{A15})$$

These expressions are useful for examining various limits of the more general result. For instance, for $q = 0$ they yield $\mathcal{R} = \pi/e^2$, in agreement with the result of Büttiker.²¹

Appendix B: Long cylinders

When the cylinder is long such that the frequency exceeds the level spacing, $md^2 \gg \omega^{-1}$, a straightforward expansion of the ac conductance is not possible since the integrand in Eq. (8) is rapidly oscillating. For simplicity, we consider the case where the spin-orbit interaction vanishes. Then the ac conductance, at zero temperature, is

$$\mathcal{G}(\omega) = \frac{e^2}{\pi\omega} \int_{E_F - \omega}^{E_F} dE \sum_q \left(1 - \frac{\zeta(1 - e^{2idk}) - ik}{\zeta(1 - e^{-2idk}) + ik} \times \frac{\zeta(1 - e^{-2idk_\omega}) + ik_\omega}{\zeta(1 - e^{2idk_\omega}) - ik_\omega} \right), \quad (\text{B1})$$

with $k_\omega \equiv \sqrt{2m(E + \omega) - q^2}$. The averaging over the rapid oscillations is carried out by integrating in the complex plane over the contour of the unit circle,

$$\begin{aligned} \frac{\pi\omega}{e^2} \mathcal{G}(\omega) &= \oint dz_1 \oint dz_2 \int_{E_F - \omega}^{E_F} dE \sum_q \left(1 - \frac{\zeta(1 - e^{z_1}) - ik}{\zeta(1 - e^{-z_1}) + ik} \times \frac{\zeta(1 - e^{-z_2}) + ik_\omega}{\zeta(1 - e^{z_2}) - ik_\omega} \right) \\ &= \int_{E_F - \omega}^{E_F} dE \sum_q \left(1 - \frac{(\zeta - ik)(\zeta + ik_\omega)}{(\zeta + ik)(\zeta - ik_\omega)} \right). \end{aligned} \quad (\text{B2})$$

The low-frequency expansion of the ac conductance now yields

$$\mathcal{C} = \frac{e^2}{2\pi} \sum_q \frac{4m\zeta}{k_\mu(k_\mu^2 + \zeta^2)}, \quad (\text{B3})$$

and

$$\mathcal{R} = \frac{\pi}{e^2} \frac{\sum_q \left(\frac{4m\zeta}{k_\mu(k_\mu^2 + \zeta^2)} \right)^2}{\left(\sum_q \frac{4m\zeta}{k_\mu(k_\mu^2 + \zeta^2)} \right)^2}, \quad (\text{B4})$$

where $k_\mu = \sqrt{2mE_F - q^2}$ (recall that at zero temperature $\mu = E_F$). For the lowest transverse mode $q = 0$ we find $\mathcal{R} = \pi/e^2$, in agreement with the result of Refs. 27.

As noted after Eq. (7), the effect of the spin-orbit interaction can be gauged out for a single-channel scatterer and therefore the result $\mathcal{R} = \pi/e^2$ holds also when the scattered electrons undergo a spin-orbit interaction.

Appendix C: The scattering matrix of a tube

In order to derive the scattering matrix for the geometry depicted in Fig. 3 we need to consider the wave functions in the scattering region $|x| < d$ and in the two leads, the regions $x \geq d$ and $x \leq -d$. In the region $|x| < d$ we choose the same one as in Appendix A, Eqs. (A2), (A3), and (A4). For the wave functions in the leads we write the Ansatz

$$\begin{aligned} \varphi_L(x, y) &= \sum_q e^{iqy} \left[e^{ik(x+d)} |c_{L,\text{in}}\rangle + e^{-ik(x+d)} |c_{L,\text{out}}\rangle \right], \quad x < -d, \\ \varphi_R(x, y) &= \sum_q e^{iqy} \left[e^{-ik(x-d)} |c_{R,\text{in}}\rangle + e^{ik(x-d)} |c_{R,\text{out}}\rangle \right], \quad x > d, \end{aligned} \quad (\text{C1})$$

where $|c_{\gamma,\text{in}}\rangle$ ($|c_{\gamma,\text{out}}\rangle$) is the incoming (outgoing) spinor in lead γ . Note that the direction of the incoming spinors is toward the central region, i.e., the scatterer.

As before, the transverse channels are not coupled and therefore we may solve the scattering matrix for a certain q . We use the boundary conditions to eliminate the spinors in the scattering region $|x| \leq d$. The first set of boundary conditions follows from the continuity of the wave functions at $x = d$,

$$\mathbf{v}_u e^{ik_u d \sigma_z} |c_u\rangle + \mathbf{v}_d e^{ik_d d \sigma_z} |c_d\rangle = |c_{R,\text{in}}\rangle + |c_{R,\text{out}}\rangle, \quad (\text{C2})$$

and the continuity of the wave functions at $x = -d$,

$$\mathbf{v}_u e^{-ik_u d \sigma_z} |c_u\rangle + \mathbf{v}_d e^{-ik_d d \sigma_z} |c_d\rangle = |c_{L,\text{in}}\rangle + |c_{L,\text{out}}\rangle, \quad (\text{C3})$$

where $k_{u,d}$ is given in Eq. (5). The second set of boundary conditions comes from the continuity of the current, at $x = d$

$$ik(|c_{L,\text{in}}\rangle - |c_{L,\text{out}}\rangle) + (2\zeta + i\alpha\sigma_y)(|c_{L,\text{in}}\rangle + |c_{L,\text{out}}\rangle) = ik_u \mathbf{v}_u \sigma_z e^{-ik_u d \sigma_z} |c_u\rangle + ik_d \mathbf{v}_d \sigma_z e^{-ik_d d \sigma_z} |c_d\rangle, \quad (\text{C4})$$

and at $x = -d$

$$ik(|c_{R,\text{in}}\rangle - |c_{R,\text{out}}\rangle) + (2\zeta - i\alpha\sigma_y)(|c_{R,\text{in}}\rangle + |c_{R,\text{out}}\rangle) = -ik_u \mathbf{v}_u \sigma_z e^{ik_u d \sigma_z} |c_u\rangle - ik_d \mathbf{v}_d \sigma_z e^{ik_d d \sigma_z} |c_d\rangle. \quad (\text{C5})$$

Once the spinors $|c_u\rangle$ and $|c_d\rangle$ are eliminated, we find

$$\begin{bmatrix} |c_{L,\text{out}}\rangle \\ |c_{R,\text{out}}\rangle \end{bmatrix} = \mathcal{S} \begin{bmatrix} |c_{L,\text{in}}\rangle \\ |c_{R,\text{in}}\rangle \end{bmatrix}, \quad \mathcal{S} = \begin{bmatrix} \mathbf{R}_{LL} & \mathbf{T}_{RL} \\ \mathbf{T}_{LR} & \mathbf{R}_{RR} \end{bmatrix}, \quad (\text{C6})$$

where

$$\begin{aligned} \mathbf{R}_{LL} &= -1 + 2ik \left(\tilde{\mathbf{G}} - \tilde{\mathbf{F}} \mathbf{G}^{-1} \mathbf{F} \right)^{-1} \tilde{\mathbf{F}} \mathbf{G}^{-1}, & \mathbf{T}_{RL} &= 2ik \left(\tilde{\mathbf{G}} - \tilde{\mathbf{F}} \mathbf{G}^{-1} \mathbf{F} \right)^{-1} \\ \mathbf{R}_{RR} &= -1 + 2ik \left(\mathbf{G} - \mathbf{F} \tilde{\mathbf{G}}^{-1} \tilde{\mathbf{F}} \right)^{-1} \mathbf{F} \tilde{\mathbf{G}}^{-1}, & \mathbf{T}_{LR} &= 2ik \left(\mathbf{G} - \mathbf{F} \tilde{\mathbf{G}}^{-1} \tilde{\mathbf{F}} \right)^{-1}. \end{aligned} \quad (\text{C7})$$

Here we have introduced the definitions

$$\begin{aligned} \mathbf{F} &= 2\zeta_L + i\alpha\sigma_y - ik - ik_u \mathbf{v}_u \sigma_z e^{-ik_u \sigma_z d} \mathbf{B}_u^{-1} - ik_d \mathbf{v}_d \sigma_z e^{-ik_d \sigma_z d} \mathbf{B}_d^{-1}, \\ \tilde{\mathbf{F}} &= 2\zeta_R - i\alpha\sigma_y - ik - ik_u \mathbf{v}_u \sigma_z e^{ik_u \sigma_z d} \mathbf{B}_u^{-1} \mathbf{A}_d - ik_d \mathbf{v}_d \sigma_z e^{ik_d \sigma_z d} \mathbf{B}_d^{-1} \mathbf{A}_u, \\ \mathbf{G} &= -ik_u \mathbf{v}_u \sigma_z e^{-ik_u \sigma_z d} \mathbf{B}_u^{-1} \mathbf{A}_d - ik_d \mathbf{v}_d \sigma_z e^{-ik_d \sigma_z d} \mathbf{B}_d^{-1} \mathbf{A}_u, \\ \tilde{\mathbf{G}} &= -ik_u \mathbf{v}_u \sigma_z e^{ik_u \sigma_z d} \mathbf{B}_u^{-1} - ik_d \mathbf{v}_d \sigma_z e^{ik_d \sigma_z d} \mathbf{B}_d^{-1}, \end{aligned} \quad (\text{C8})$$

with

$$\mathbf{A}_l = \mathbf{v}_l e^{-2ik_l \sigma_z d} \mathbf{v}_l^{-1}, \quad \mathbf{B}_l = \mathbf{v}_l e^{-ik_l \sigma_z d} - \mathbf{A}_l \mathbf{v}_l e^{ik_l \sigma_z d}, \quad (\text{C9})$$

where $l=u$ or d , and $l \neq l'$.

* Electronic address: rotshteil@post.bgu.ac.il

¹ R. Winkler, *Spin-Orbit Coupling Effects in Two-Dimensional Electron and Hole Systems* (Springer, Berlin, 2003).

² E. I. Rashba, Fiz. Tverd. Tela (Leningrad) **2**, 1224 (1960) [Sov. Phys. Solid State **2**, 1109 (1960)]; Y. A. Bychkov and E. I. Rashba, J. Phys. C **17**, 6039 (1984).

³ J. Nitta, T. Akazaki, H. Takayanagi, and T. Enoki, Phys. Rev. Lett. **78**, 1335 (1997).

⁴ G. Engels, J. Lange, Th. Schäpers, and H. Lüth, Phys. Rev. B **55**, 1958(R) (1997); Th. Schäpers, J. Knobbe, and

V. A. Guzenko, Phys. Rev. B **69**, 235323 (2004).

⁵ Y. Meir, Y. Gefen, and O. Entin-Wohlman, Phys. Rev. Lett. **63**, 798 (1989).

⁶ A. Aharony, Y. Tokura, G. Z. Cohen, O. Entin-Wohlman, and S. Katsumoto, Phys. Rev. B **84**, 035323 (2011).

⁷ F. Kuemmeth, S. Ilani, D. C. Ralph, and P. L. McEuen, Nature (London) **452**, 448 (2008); K. Flensberg, and C. M. Marcus, Phys. Rev. B **81**, 195418 (2010).

⁸ C. Feuillet-Palma, T. Delattre, P. Morfin, J.-M. Berroir, G. Fève, D. C. Glattli, B. Plaças, A. Cottet, and T. Kontos, Phys. Rev. B **81**, 115414 (2010).

- ⁹ Z. Xie, T. Z. Markus, S. R. Cohen, Z. Vager, R. Gutierrez, and R. Naaman, *Nano Lett.* **11**, 4652 (2011).
- ¹⁰ T. Ando, *J. Phys. Soc. Jpn.* **69**, 1757 (2000).
- ¹¹ L. J. Lauhon, M. S. Gudiksen, D. Wang, and C. M. Lieber, *Nature (London)* **420**, 57 (2002); J. Noborisaka, J. Motohisa, S. Hara, and T. Fukui, *Appl. Phys. Lett.* **87**, 093109 (2005); G. Zhang, K. Tatenno, T. Sogawa, and H. Nakano, *Appl. Phys. Express* **1**, 064003 (2008).
- ¹² J. W. W. van Tilburg, R. E. Algra, W. G. G. Immink, M. Verheijen, E. P. A. M. Bakkers, and L. P. Kouwenhoven, *Semicond. Sci. Technol.* **25**, 024011 (2010); R. Popovitz-Biro, A. Kretinin, P. Von Huth, and H. Shtrikman, *Cryst. Growth Des.* **11**, 3858 (2011).
- ¹³ T. Rieger, M. Luysberg, T. Schäpers, D. Grützmacher, and M. I. Lepsa, *Nano Lett.* **12**, 5559 (2012); C. Blömers, T. Rieger, P. Zellekens, F. Haas, M. I. Lepsa, H. Hardtdegen, Ö. Gül, N. Demarina, D. Grützmacher, H. Lüth, and T. Schäpers, *Nanotechnology* **24**, 035203 (2013).
- ¹⁴ M. Jung, J. S. Lee, W. Song, Y. H. Kim, S. D. Lee, N. Kim, J. Park, M.-S. Choi, S. Katsumoto, H. Lee, and J. Kim, *Nano Lett.* **8**, 3189 (2008); Ö. Gül, N. Demarina, C. Blömers, T. Rieger, H. Lüth, M. I. Lepsa, D. Grützmacher, and T. Schäpers, *Phys. Rev. B* **89**, 045417 (2014).
- ¹⁵ O. Entin-Wohlman, A. Aharony, Y. Tokura, and Y. Avishai, *Phys. Rev. B* **81**, 075439 (2010).
- ¹⁶ T. O. Rosdahl, A. Manolescu, and V. Gudmundsson, *Phys. Rev. B* **90**, 035421 (2014).
- ¹⁷ M. Büttiker, A. Prêtre, and H. Thomas, *Phys. Rev. Lett.* **70**, 4114 (1993).
- ¹⁸ M. Büttiker, *Phys. Rev. B* **46**, 12485 (1992).
- ¹⁹ For example, G. Hackenbroich and H. Weidenmüller, *Phys. Rev. B* **53**, 16379 (1996).
- ²⁰ J. Gabelli, J. M. Berrior, G. Féve, B. Plaçais, Y. Jin, B. Etienne, and D. C. Glatthli, *Science* **313**, 499 (2006).
- ²¹ M. Büttiker, H. Thomas, and A. Prêtre, *Phys. Lett. A* **180**, 364 (1993).
- ²² A. Prêtre, H. Thomas, and M. Büttiker, *Phys. Rev. B* **54**, 8130 (1997).
- ²³ M. Khodas, A. Shekhter, and A. M. Finkel'stein, *Phys. Rev. Lett.* **92**, 086602 (2004); A. Shekhter, M. Khodas, and A. M. Finkel'stein, *Phys. Rev. B* **71**, 125114 (2005); P. G. Silverstrov and E. G. Mishchenko, *Phys. Rev. B* **74**, 165301 (2006).
- ²⁴ J. S. Langer and V. Ambegaokar, *Phys. Rev.* **121**, 1090 (1961).
- ²⁵ T. Taniguchi and M. Büttiker, *Phys. Rev. B* **60**, 13814 (1999).
- ²⁶ M. Büttiker, *J. Low Temp. Phys.* **118**, 519 (2000).
- ²⁷ C. Mora and K. Le Hur, *Nature Physics* **6**, 697 (2010); M. Filippone and C. Mora, *Phys. Rev. B* **86**, 125311 (2012).
- ²⁸ Y. Imry, *Introduction to Mesoscopic Physics*, 2nd ed. (Oxford University Press, Oxford, 2002).
- ²⁹ E. A. Rothstein, O. Entin-Wohlman, and A. Aharony, *Phys. Rev. B* **79**, 075307 (2009).
- ³⁰ G. B. Lesovik, *JETP Lett.* **49**, 594 (1989).
- ³¹ R. Aguado, and L. P. Kouwenhoven, *Phys. Rev. Lett.* **84**, 1986 (2000).
- ³² U. Gavish, Y. Levinson, and Y. Imry, *Phys. Rev. Lett.* **87**, 216807 (2001); *Phys. Rev. B* **62**, R10637 (2000).
- ³³ N. Gabdank, E. A. Rothstein, O. Entin-Wohlman, and A. Aharony, *Phys. Rev. B* **84**, 235435 (2011).
- ³⁴ F. T. Smith, *Phys. Rev.* **118**, 349 (1960).
- ³⁵ S. A. van Langen, P. G. Silverstrov, and C. W. J. Beenakker, *Superlattices and Microstructures* **23**, 691 (1998).
- ³⁶ A. I. Rahachou and I. V. Zozoulenko, *Appl. Opt.* **43**, 1761 (2004).
- ³⁷ A. K. Hüttel, G. A. Steele, B. Withkamp, M. Poot, L. P. Kouwenhoven, and H. S. J. van der Zant, *Nano Lett.* **9**, 2547 (2009); E. A. Laird, F. Pei, W. Tang, G. A. Steele, and L. P. Kouwenhoven, *Nano Lett.* **12**, 193 (2012).
- ³⁸ A. K. Jonscher, *J. Chem. Soc., Faraday Trans. 2* **82**, 75 (1986); Y. Fu and S. C. Dudley, *Phys. Rev. Lett.* **70**, 65 (1992); M. Ershov, H. C. Liu, L. Li, M. Buchanan, Z. R. Wasilewski, and A. K. Jonscher, *IEEE Trans. Electron Devices* **45**, 2196 (1998); Y. P. Zhao, B. -Q. Wei, P. M. Ajayan, G. Ramanath, T. -M. Lu, G. -C. Wang, A. Rubio, and S. Roche, *Phys. Rev. B* **64**, 201402 (2001); Y. Wei, X. Zhao, B. Wang, and J. Wang, *J. Appl. Phys.* **98**, 086103 (2005); S. Salahuddin and S. Datta, *Nano Lett.* **8**, 405 (2008).